Article

Integrating SAR and Optical Data for Aboveground Biomass Estimation of Coastal Wetlands Using Machine Learning: Multi-Scale Approach

Mohammadali Hemati [1][iD]**, Masoud Mahdianpari** [1,2,*][iD]**, Hodjat Shiri** [3][iD] **and Fariba Mohammadimanesh** [2]

1 Department of Electrical and Computer Engineering, Memorial University of Newfoundland, St. John's, NL A1C 5S7, Canada; mhemati@mun.ca
2 C-Core, St. John's, NL A1B 3X5, Canada; fm7550@mun.ca
3 Civil Engineering Department, Faculty of Engineering and Applied Sciences, Memorial University of Newfoundland, St. John's, NL A1B 3X7, Canada; hshiri@mun.ca
* Correspondence: m.mahdianpari@mun.ca

Abstract: Coastal wetlands encompass diverse ecosystems such as tidal marshes, mangroves, and seagrasses, which harbor substantial amounts of carbon (C) within their vegetation and soils. Despite their relatively small global extent, these wetlands exhibit carbon sequestration rates on par with those observed in terrestrial forests. The application of remote sensing technologies offers a promising means of monitoring aboveground biomass (AGB) in wetland environments. However, the scarcity of field data poses a significant challenge to the utilization of spaceborne data for accurate estimation of AGB in coastal wetlands. To address this limitation, this study presents a novel multi-scale approach that integrates field data, aerial imaging, and satellite platforms to generate high-quality biomass maps across varying scales. At the fine scale level, the AVIRIS-NG hyperspectral data were employed to develop a model for estimating AGB with an exceptional spatial resolution of 5 m. Subsequently, at a broader scale, large-scale and multitemporal models were constructed using spaceborne Sentinel-1 and Sentinel-2 data collected in 2021. The Random Forest (RF) algorithm was utilized to train spring, fall and multi-temporal models using 70% of the available reference data. Using the remaining 30% of untouched data for model validation, Root Mean Square Errors (RMSE) of 0.97, 0.98, and 1.61 Mg ha^{-1} was achieved for the spring, fall, and multi-temporal models, respectively. The highest R-squared value of 0.65 was achieved for the multi-temporal model. Additionally, the analysis highlighted the importance of various features in biomass estimation, indicating the contribution of different bands and indices. By leveraging the wetland inventory classification map, a comprehensive temporal analysis was conducted to examine the average and total AGB dynamics across various wetland classes. This analysis elucidated the patterns and fluctuations in AGB over time, providing valuable insights into the temporal dynamics of these wetland ecosystems.

Keywords: aboveground biomass; coastal wetlands; tidal marsh; AVIRIS-NG; multispectral; SAR; hyperspectral

1. Introduction

Coastal wetlands include tidal marshes, mangroves, and seagrasses, all of which contain significant amounts of carbon (C) in their soils and vegetation [1]. Despite their smaller global coverage [2], these stores sequester atmospheric carbon at rates comparable to those of terrestrial forests. Carbon can be sequestered by tidal marshes at an average rate of 1–2 Mg C per hectare per year [3]. As a result of human activities, including coastal development, agriculture, and sea-level rise caused by climate change and extreme weather events, these wetlands are being converted to open water or other types of land cover at a rate of 1–2% worldwide [4,5]. There are estimates that range from 21–760 million Mg CO$_2$ equivalents per year that result from this land use change, which contributes to climate

change [6]. The possibility of coastal wetlands mitigating climate change has received considerable attention in recent years due to their large carbon stocks, high carbon sequestration rates, and the possibility that human activities, such as conversion and degradation, could increase greenhouse gas (GHG) emissions [7,8]. Thus, several entities have expressed a desire to manage coastal wetland blue carbon [9]. Coastal wetland restoration and conservation projects can now receive carbon credits for reducing greenhouse gas emissions [10] through voluntary carbon markets such as the Verified Carbon Standard (VCS). In addition to facilitating the reduction of greenhouse gas emissions, this will provide an incentive to restore and conserve coastal wetlands as well as finance such projects.

In spite of the requirement that five carbon pools (soils, above- and below-ground biomass, dead wood, and litter) be reported, due to insufficient data on biomass, dead wood, and litter, the initial coastal wetlands inventory only accounted for changes in soil carbon stocks, which is the largest carbon pool for tidal marshes. As emergent marshes account for over 80% of all tidal wetlands in the CONUS [11,12], estimating carbon emissions from coastal lands may require an understanding of their biomass. The IPCC, 2003, reports that higher spatial and temporal resolution data, as well as more disaggregated data, are needed to include tidal marsh biomass in coastal wetlands GHG inventories, particularly at a Tier 2 level [13]. A biomass carbon stock can also assist in verifying emissions reductions for projects participating in voluntary carbon markets [6]. These objectives can be achieved through remote sensing-based maps of tidal marshes, encompassing their extents as well as their carbon stocks [14]. With remote sensing data, it is possible to evaluate spatial and temporal changes in biomass in vast regions using a repeatable and standardized method, fulfilling a vital role in GHG inventories and monitoring carbon mitigation efforts [15]. For tidal marsh GHG inventories in the United States, the NOAA Office for Coastal Management [16] uses the Coastal Change Analysis Program (C-CAP) dataset as the primary spatial dataset. In 1996, 2001, 2006, and 2010, CONUS produced a dataset in four to five-year intervals. Based on Landsat imagery, C-CAP provides 30 m resolution coastal lands maps, along with wetland classifications. Forested, scrub-shrub, and emergent marshes are all classified according to their salinity, and into estuarine and palustrine wetlands. C-CAP maps were generated using Landsat data, which may provide additional information on vegetation conditions.

With the availability of free, preprocessed satellite and aerial imagery covering national to global areas, recent advances in remote sensing technology have made it possible to monitor the Earth's surface on a large scale [17]. Landsat's satellite image catalog is now georeferenced and calibrated as a surface reflectance product that can be used for biomass estimation in regions where data are limited [18]. European Space Agency (ESA) provides 10 m globally free access Synthetic Aperture Radar (SAR) and multispectral data through Copernicus Sentinel-1 and Sentinel-2 program [19]. Sentinel data with higher spatiotemporal resolution, proved to be a great solution for wetland monitoring, especially in large scale [20,21]. Using cloud computing platforms like Google Earth Engine (GEE), global products such as global forest cover change maps and global surface water inundation maps can be produced using a petabyte catalog of satellite images and geospatial datasets and a massively parallel, distributed runtime engine [22,23]. Remote sensing has become increasingly accessible due to these advances, providing a powerful tool for monitoring and assessing surface changes [24–26]. Recent years have seen a number of attempts to estimate the biomass of tidal marshes using remote sensing techniques in different regions, including those in South Africa [27], Argentina [28], and throughout the United States [29–31]. Previous studies with empirical models are often calibrated to specific locations and years based on the unique characteristics of local ecosystems, such as plant community composition, water depth, and soil types, even though they have successfully estimated tidal marsh biomass with an error rate below 20%. They noted that these models have significant limitations in terms of scaling [32]. A variation in canopy architecture or leaf traits can limit the ability of empirical models of biophysical features, such as biomass, to be applied to other regions. As a result of these differences, vegetation indexes, and biomass levels can

be different across plant communities due to discrepancies in optical properties [33–35]. A tidal marsh rush, a sedge, or a grass's vertical stem morphology can cause light to scatter and absorb in the space between the plants, resulting in a lower canopy reflectance [36,37]. Distichlis spicata, for example, has horizontal leaves, which supports the strong correlation between biomass and vegetation indexes such as NDVI [38]. Scaling empirical models to other regions and plant communities can be challenging because of these differences in optical properties.

Spectral data with moderate and coarse spatial resolution have been used for biomass mapping before [39,40]. In wetland regions, the integration of SAR and optical data have proven to be useful since radar data include information regarding the structure and water content of the target [41]. Therefore, recent studies increased the accuracy of the wetland biomass mapping through usage of multi-source earth observation data [42–47]. LiDAR and hyperspectral sensors, also, have been used besides the spaceborne platforms for estimation of wetland biomass with high details and accuracy [48,49]. Studies using airborne platforms, such as UAV, provided biomass maps in wetlands with high accuracy and very high spatial resolution [50,51]. Most of the airborne datasets are acquired during the field campaigns, at the same time frame with the in-situ datasets. However, they are costly and lack the spatial coverage and temporal resolution of the spaceborne platforms, such as Sentinel-1/2. Leveraging the capability of both airborne and space-based observation, a multi-scale and multi-platform approach was developed in this study in order to: demonstrate the capabilities of remote sensing technologies, multi-source earth observation data, and advancements in cloud computing platforms for monitoring biomass in coastal wetlands on a large scale over the state of Louisiana; develop a scalable multi-level model to estimate the AGB over a small and large scale based on both aerial and satellite data and machine learning techniques, and perform a seasonality analysis to understand the intra-annual pattern of the AGB and wetland phenology using a multi-temporal model.

Our study examines the development of remote sensing models regardless of differences in vegetation structure and composition among estuaries. Through leveraging a multi-scale and multi-platform approach, the performance of models is improved and the uncertainties in estimates of AGB are assessed. This study examines the potential benefits of using multi-source earth observation data to improve estimations of vegetation cover and biomass by combining Sentinel-1 SAR backscatter with Sentinel-2 multispectral data. Following the development of the multi-temporal model, we examine the model's capability of distinguishing regional and subregional differences between mean and total AGB across regions and wetland types mapped in the study area.

2. Method

2.1. Study Area

The study area is the coastal wetlands located in the southern region of Louisiana. This area encompasses the Watershed Boundary regions designated by the United States Geological Survey (USGS) at Level-4 classification. Specifically, our research encompasses the hydrologic units spanning the lower Mississippi River and the coastal areas of Louisiana. By targeting these particular regions, we aim to provide a comprehensive analysis of the ecological dynamics and hydrological processes within the coastal wetlands of this unique and critical environment. This region contains the Mississippi River Delta (MRD) and Western Louisiana Delta (WLD). During the 1940s, a river diversion was implemented to control channel flow to Morgan City, reducing the risk of flooding. In 1973, the WLD became subaerial as a result of a river diversion implemented in 1941. In addition to receiving about 30% of the water discharge from the Mississippi River, the Atchafalaya River outlet accounts for 10% of its flow [52]. WLD morphology is influenced by a constant supply of sediment, floods caused by rivers, hurricanes, and cold fronts, and biological processes like organic matter production. In coastal deltaic floodplains, like WLD, tidal freshwater wetland species are grouped according to the elevations of the marsh, which range from subtidal to supratidal in hydrogeomorphic zones. As a natural observatory for

assessing hypotheses about coastal deltaic wetlands and their trajectory and sustainability as an adaptation strategy to relative sea level rise, WLD has a number of geomorphic characteristics. An overview of the study area region is illustrated in Figure 1. This area includes the southern coastal wetlands of Louisiana, and the U.S. wetland inventory by U.S. Fish and Wildlife Service is shown, along with Atchafalaya and Terrebonne basins and field data sampling sites.
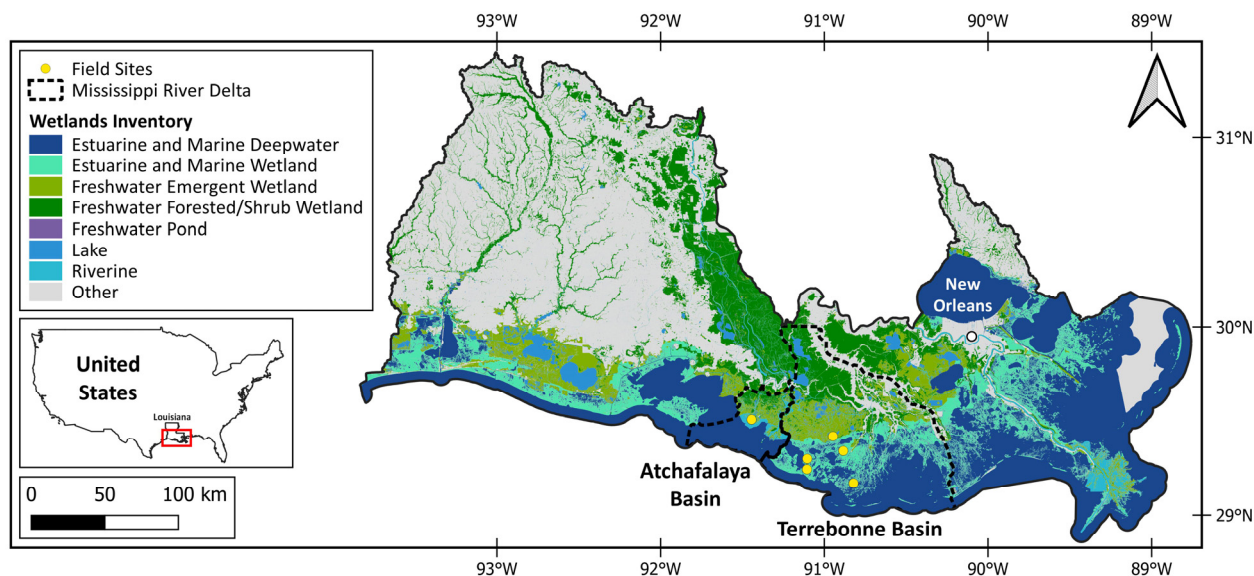

Figure 1. An overview of the study area.

2.2. Satellite Datasets

To improve the accuracy of AGB estimation, a diverse set of earth observation data sources was employed. Spaceborne data, including Sentinel-1, -2, and SRTM were accessed and processed within the GEE. As part of the Copernicus program of the ESA, Sentinel-2 is a high-resolution optical imaging mission with open-access data. It provides global coverage of Earth's surface at regular intervals by covering 290 km of swath and five days at the equator. The satellite's spatial resolution varies between different spectral bands, with values of 10 m (visible and NIR), 20 m (red edge and SWIR), and 60 m (aerosols and water vapor). The data is acquired with 12-bit radiometric resolution and processed by the Level-2A processor, which corrects for atmospheric effects, such as Rayleigh scattering, aerosol scattering, and absorption by water vapor and ozone [53]. Moreover, the processor applies scene classification algorithms to identify land cover types and mask out unwanted features such as clouds and shadows. In this study, Level-2A surface reflectance data are utilized to enhance the regression results. Land cover types and wetlands exhibit spectral responses that are independent of time and place, with minimal effects of the atmosphere on surface reflectance.

In addition, Sentinel-1, which is also part of the Copernicus program and uses SAR imaging to collect data, is another important source of data for this study. With a frequency of 5.405 GHz, the satellite's SAR sensor operates in both single and dual polarization modes and can return to the equator 12 days at a time [54]. Ground Range Detected (GRD) data acquired with a spatial resolution of 10 m are used in this study in a dual-band cross-polarization mode (vertical transmit/horizontal receive), using the Interferometric Wide Swath (IW) mode. Using the Sentinel-1 Toolbox, data have been calibrated radiometrically, thermal noise has been removed, and terrain has been corrected. To reduce the speckle, a temporal median filter has been applied to match with the timeframe of the Sentinel-2 data. In addition, the study employed a 30 m SRTM digital elevation model (DEM) with slope and aspect features extracted. The integration of these data should improve the accuracy and reliability of the AGB estimation process. Land surface features can be identified using

Sentinel-2 data, while vegetation structures can be characterized using Sentinel-1 data. Figure 2 shows the different earth observation data used in this study, including vertically transmitted and received backscatter of Sentinel-1, RGB true-color image of the median composite of Sentinel-2, SRTM DEM data, and AVIRIS-NG footprint.
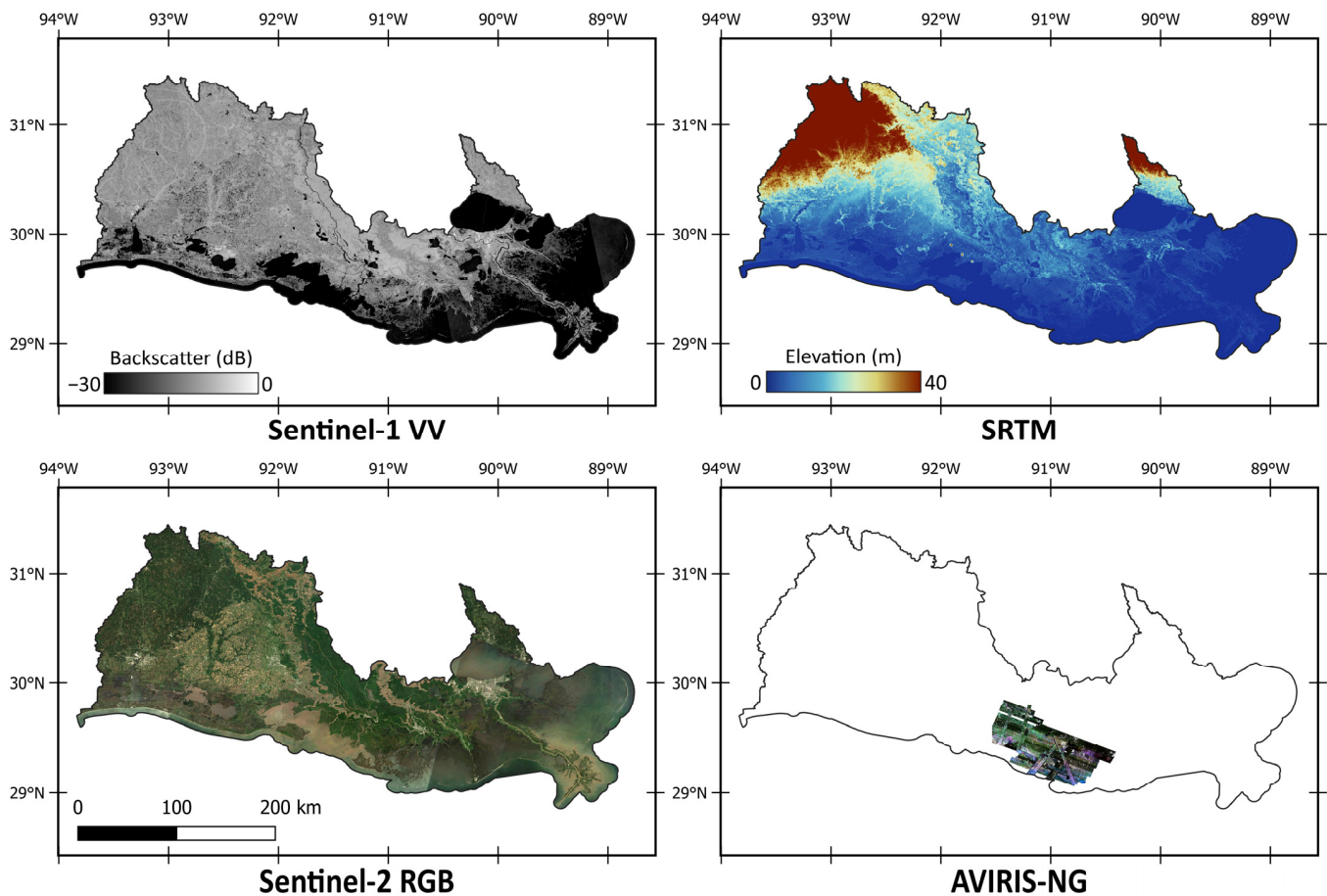

Figure 2. Different earth observation data are used for AGB estimation.

2.3. Field and Aerial Dataset

In this study, the Delta-X mission, a NASA Earth Venture Suborbital-3 project spanning five years, is examined in relation to the MRD in the United States. Deltas and associated wetlands around the Mississippi River suffer from drowning due to sea-level rise and decreased sediment inputs in various regions of the delta. Therefore, Delta-X seeks to identify which areas will prosper and which will decline further as the environment degrades. As part of the Delta-X mission, airborne and in situ data are collected and analyzed, and models are integrated and validated. Ultimately, the goal is to predict deltaic land loss or gain in the future [55]. Wetland ecosystem studies in the MRD and beyond will be transformed by the Delta-X mission. In order to better understand the dynamics and functions of these ecosystems, researchers can use advanced data acquisition and data analysis techniques. In addition, the Delta-X mission provides information about how wetland ecosystems can be preserved and managed in the face of environmental degradation, with implications for preventing global climate change. Delta-X provides a comprehensive in-situ dataset of samples collected from herbaceous wetlands in southeastern coastal Louisiana in 2021 that provide total carbon, total nitrogen, and total phosphorus contents, along with biomass values. The field campaigns were carried out during two distinct periods: from 19 March 2021, to 2 April 2021, corresponding to the spring season, and from 19 August 2021, to 27 August 2021, representing the fall season. These timeframes were chosen to capture the seasonal variations in vegetation dynamics and aboveground biomass within the study area. Sam-

ples were collected from aboveground biomass (AGB) and necromass (AGN) located in the Atchafalaya and Terrebonne basins. Atchafalaya basin measurements were taken at three sites, and Terrebonne basin measurements were taken at three more sites [56]. At every herbaceous wetland location, a transect was set up perpendicular to the wetland boundary to encompass various hydrogeomorphic zones, including supratidal and intertidal areas. Within each hydrogeomorphic zone, two sampling stations were established at intervals of 30 m, aligned parallel to the wetland edge. Within these stations, vegetation structure was assessed, and AGB was collected within duplicate plots measuring 0.25 square meters each. These plots were positioned 5 m apart at each sampling station, enabling comprehensive assessment and replication of measurements across the wetland site. For further analysis, all AGB plant material within each plot was clipped at soil level, placed in plastic bags, and transported to the laboratory. To represent the salinity gradient within both basins, herbaceous wetland sites spanning freshwater, brackish, and saline environments were selected. For the spring season, the number of AGB samples was 86 and for fall was 96. AGB values were reported in gram per square meter (g m^{-2}) and other nutrients were reported in milligram per gram (mg g^{-1}).

In the course of spring and autumn 2021, the National Aeronautics and Space Administration's (NASA) Airborne Visible Infrared Imaging Spectrometer-Next Generation (AVIRIS-NG) gathered data from selected areas within the Atchafalaya and Terrebonne basins situated in coastal Louisiana. The Delta-X campaign, a collaborative initiative comprising both airborne and field operations, was conducted in the MRD. AVIRIS-NG, a high signal-to-noise ratio (SNR) pushbroom spectral mapping system, was specifically engineered for advanced spectroscopy, succeeding the Classic Airborne Visible Infrared Imaging Spectrometer (AVIRIS-C) [57]. The instrument encompasses the full solar-reflected spectrum, ranging from 380 to 2510 nm, utilizing a single Focal Plane Array (FPA) at approximately 5 nm spectral sampling. AVIRIS-NG's sensor possesses a 1-milliradian instantaneous field of view, thereby yielding altitude-dependent ground sampling distances that span from sub-meter to 20 m scales. Its detector consists of a 640 × 480-pixel array, from which standard products are derived via the sensor's 600 cross-track spatial samples and 425 spectral samples. Each data collection, referred to as a "flight line," constitutes a continuous strip of pushbroom information typically captured within 1 to 10 minutes. To produce a comprehensive map of the targeted area, multiple aircraft overflights amass data in these strips, encompassing the region of interest. Subsequent to each AVIRIS-NG flight line, the data underwent atmospheric correction to generate Hemispherical-Directional surface reflectance datasets [58]. Further adjustments were made to account for bidirectional reflectance distribution function (BRDF) effects and sun-glint across land and water pixels, respectively [59,60].

2.4. AGB Regression Models

In addressing the challenge of modeling AGB with limited ground data, this study leveraged a combination of satellite and airborne datasets to enhance predictive accuracy. Initially employing Sentinel-1 and -2 data, efforts were made to develop a regression model; however, the outcomes proved suboptimal, due to the very limited number of ground samples and insufficient spatial resolution of Sentinel platforms. Consequently, the study turned to AVIRIS-NG data, notable for its superior spatial and spectral resolution, to refine the modeling process within a small-scale context. Leveraging the enhanced resolution of AVIRIS-NG, the dataset was sampled strategically to train comprehensive models applicable to larger-scale assessments utilizing spaceborne data. By integrating high-resolution AVIRIS-NG data to inform the modeling process at a localized level, and subsequently extrapolating insights to broader spatial extents using spaceborne datasets, this methodology endeavors to optimize predictive accuracy in AGB estimation. In order to accurately estimate biomass, this study employed a comprehensive approach encompassing multiple classification scenarios that incorporated diverse scales and temporal information. The intricate flowchart of the research methodology, depicted in Figure 3, provides a visual

representation of the sequential steps involved in the investigation. These steps encompass data access, preprocessing procedures, feature extraction techniques, machine learning algorithms, and rigorous model evaluation protocols.
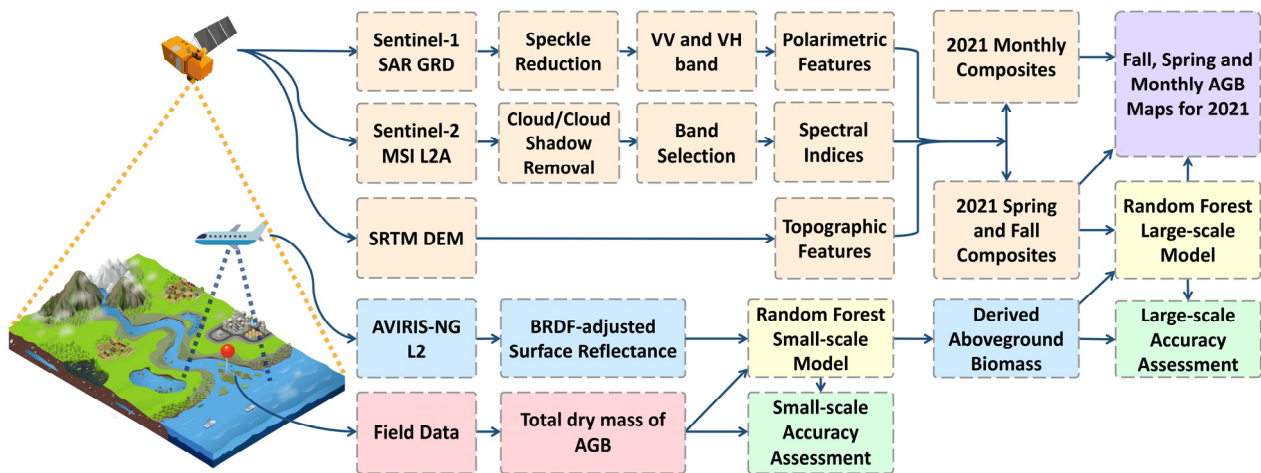

Figure 3. Flowchart of the proposed method. Boxes are color-coded with orange for spaceborne, blue for airborne, and red for ground information. Yellow boxes denote RF models, green indicates validation, and purple signifies results.

At the first level, to enhance the distribution and number of the samples for large-scale modeling, AVIRIS-NG data were used. This hyperspectral data includes much higher spectral information compared to Sentinel-2 multispectral data, in addition to much higher spatial resolution of 5 m. There have been several studies using AVIRIS-NG besides Sentinel spaceborne data to enhance the produced results [61–63]. RF is a robust classifier and regression method for wetland classification and regression [64]. RF, an ensemble learning method, works by constructing multiple decision trees during the training phase and aggregating their results to arrive at the final decision [65]. The algorithm offers robust regression capabilities for biomass estimation due to its inherent ability to handle high-dimensional and noisy data, as well as its capacity to model complex relationships between variables, which are commonly encountered in remote sensing datasets, such as Sentinel-1 and Sentinel-2. The RF model's ability to capture diverse data sources and their intricate interactions allow for improved accuracy and reduced overfitting compared to single decision tree methods. A preliminary model was developed using a RF model, that was trained using the AVIRIS-NG Level-2 BRDF-adjusted Surface Reflectance data with 70% of the ground-truth AGB samples. To train this model, cloud screened and atmospherically corrected AVIRIS-NG images were sampled using the field data from spring and fall seasons, with all the hyperspectral bands. This model then was assessed with the remaining 30% of the reference data and achieved 293.83 g m^{-2} Mean Absolute Error (MAE). AVIRIS-NG Level-3 derived AGB data were also made available by the Delta-X team with slightly better quality, which was used to train the large-scale model in the next level [66]. Pixel reflectance spectra, adjusted and aligned with AGB field measurements of herbaceous vegetation from both spring and fall 2021 collections, served as the basis for developing this RF model to estimate the AGB of at the small-scale [56]. Employing visible-shortwave infrared reflectance values as independent variables, a RF regression model was constructed for AGB estimation. Additional adjustments were made to the input spectra and mosaic imagery, specifically within the 880–1000 nm and 1080–1200 nm bands. These corrections interpolated reflectance where water vapor absorption generated excessive noise, utilizing a conditional Gaussian interpolation algorithm trained on the EMIT vegetation spectral library [67]. In order to apply the small-scale AGB model to the AVIRIS-NG data, the spring and fall mosaics for both Atchafalaya and Terrebonne Basins underwent classification to differentiate herbaceous vegetation from forests, floating

aquatic vegetation, soil, water, clouds, and cloud shadows. Subsequently, the regression model was implemented on the image mosaics corresponding to the classified herbaceous wetland pixels. The final products were then transformed into megagrams per hectare (Mg ha^{-1}) units. This model was assessed using a leave-one-out cross-validation method and achieved 257.30 g m^{-2} MAE. The resulting AVIRIS-NG Level-3 derived AGB maps only cover a small region, with large data gaps due to clouds, noises, and other masked pixels.

On the next level, the resulting AVIRIS-NG Level-3 derived AGB data was used to train the large-scale model. Sentinel-2 surface reflectance data was accessed within the GEE from timeframes matching field campaigns. All Sentinel-2 images with less than 20% cloud coverage during spring and fall timeframes were masked using the QA60 cloud mask available in the metadata of Sentinel-2 data. In addition, a secondary aerosol mask was applied to the images using a threshold on the aerosol band. Finally, a cloud-free seasonal composite was created using a median filter. From the Sentinel-2 seasonal median composite image, RGB, NIR, Red-edge, and SWIR bands were used for AGB estimation. In addition to spectral bands, spectral indices, including NDWI, NDVI, GNDVI, RVI, NDBI, NBR, BI, SAVI, EVI, NDSI, and RENDVI were extracted using spectral bands (Table 1). These indices were chosen based on previous studies on wetlands.

Table 1. Features extracted from Sentinel-1 and -2.

	Feature	Formula
Sentinel-2	Normalized Difference Water Index	$NDWI = \frac{(G-NIR)}{(G+NIR)}$
	Normalized Difference Vegetation Index	$NDVI = \frac{(NIR-R)}{(NIR+R)}$
	Green Normalized Difference Vegetation Index	$GNDVI = \frac{(NIR-G)}{(NIR+G)}$
	Ratio Vegetation Index	$RVI = \frac{RE2}{R}$
	Normalized Difference Built-Up Index	$NDBI = \frac{(SWIR1-N)}{(SWIR1+N)}$
	Normalized Burn Ratio	$NBR = \frac{(NIR-S2)}{(NIR+S2)}$
	Bare Soil Index	$BI = \frac{(SWIR1+R)-(N+B)}{(SWIR1+R)+(NIR+B)}$
	Soil-Adjusted Vegetation Index (*L = 0.5*)	$SAVI = \frac{(1.0+L)\times(NIR-R)}{NIR+R+L}$
	Enhanced Vegetation Index (*g = 2.5, C1 = 6, C2 = 7.5*)	$EVI = \frac{g\times(NIR-R)}{NIR+(C1\times R)-(C2\times B)+L}$
	Normalized Difference Snow Index	$NDSI = \frac{(G-SWIR1)}{(G+SWIR1)}$
	Red Edge Normalized Difference Vegetation Index	$ENDVI = \frac{(RE2-RE1)}{(RE2+RE1)}$
Sentinel-1	Span or Total Scattering Power	$|S_{VV}|^2 + |S_{VH}|^2$
	Ratio	$\frac{|S_{VV}|^2}{|S_{VH}|^2}$

Sentinel-1 GRD data was also accessed from GEE for the study area region. Backscattering coefficients in VV and VH polarizations were used, in addition to span and ratio indices extracted from the SAR data (Table 1). Finally, SRTM elevation data were added with the slope and aspect topographic features to create the data cube for the regression. The stacked data was sampled using the AVIRIS-NG Level-3 derived AGB using a random sampling method. Since the small-scale model was masked, only AGB values for wetlands and associated vegetations are used in sampling stage for large-scale model. Three different regression scenarios were implemented for the large-scale model. A separate RF model was trained in GEE for spring, fall, and multi-temporal AGB estimation. Seasonal models (i.e., spring and fall) were developed using samples from only one season. The multitemporal model was developed using sample data from both seasons. a trial-and-error approach led to the selection of 500 trees as the optimal number for the data at hand, strik-

ing a balance between model complexity and predictive performance while minimizing the risk of overfitting. To apply the models on the composite median images for spring, fall, and monthly maps, a low NDVI threshold was applied on the images so that unwanted areas, including upland land cover classes and water inundated areas are masked. This is due to the fact that Sentinel-1 and SRTM do not provide data for water inundated regions and also in this way the effect of erosion and sedimentation is minimized. Of sampled data, 70% was used for training the model, and the remaining 30% was used for cross-validation of the model. RMSE and R-square were calculated based on the comparison of the predicted values from the models and observed values from AVIRIS-NG Level-3 derived AGB for the training and testing sampled data to assess the performance of the models. RMSE measures the average magnitude of the differences between the observed and predicted values and provides an indication of the model's accuracy. R-squared, on the other hand, assesses the proportion of the variance in the observed data that is explained by the model, representing its goodness of fit.

3. Results

3.1. Model Assessment

The estimated AGB was evaluated using the 30% untouched test data, separately for the spring, fall, and multi-temporal models. Figure 4 illustrates this assessment through a scatter plot, demonstrating the strong agreement and integrity between the observed and predicted AGB values. Additionally, a fitted line with 95% intervals is depicted in the figure, indicating confidence in the predictions. To further quantify the performance of the regression models, two metrics were employed: RMSE and R-squared. Table 2 shows the evaluation metrics of the models. For the spring model, the RMSE was determined to be 0.97 Mg ha^{-1}, indicating a relatively small average deviation between the predicted and observed AGB values. The corresponding R-squared value was 0.45, suggesting that the model explains 45% of the variance in the observed data. Similarly, for the fall model, the RMSE was 0.98 Mg ha^{-1}, with an R-squared value of 0.36. As for the multi-temporal model, the RMSE was 1.6 Mg ha^{-1}, while the R-squared value was 0.65. Interpreting the RMSE values, lower values indicate higher accuracy and better agreement between the predicted and observed AGB values. The R-squared values indicate the extent to which the model captures the variability in the observed data, with values closer to 1 indicating a stronger relationship. Therefore, the evaluation results suggest that the multi-temporal model performed relatively better, with higher R-squared and slightly higher RMSE values compared to the spring and fall models. The out-of-the-bag (OOB) error is a valuable metric used in ensemble learning methods such as RF. It quantifies the prediction accuracy of the model by measuring the error rate on the instances that were not used during the training process. The OOB error serves as an internal validation measure, providing an estimate of the model's performance without the need for additional validation data.

Table 2. Number of samples and evaluation metrics for the produced maps.

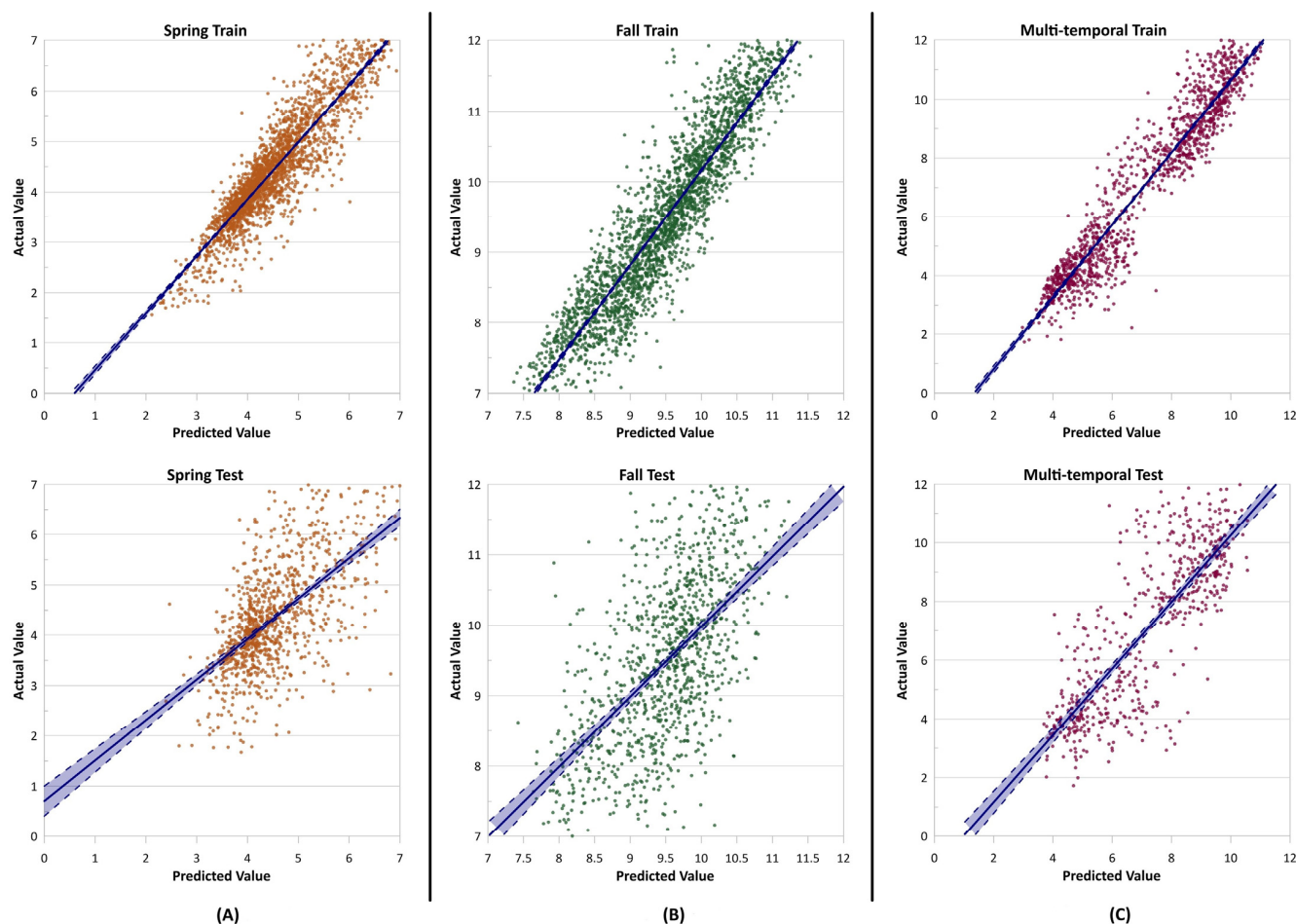|	**Spring**	**Fall**	**Multi-Temporal**
Training Samples	2610	2619	1269
Test Samples	1105	1082	921
OOB Error (Mg ha^{-1})	0.97	1.01	1.73
Training RMSE (Mg ha^{-1})	0.55	0.57	0.99
Training R-squared	0.85	0.85	0.91
Test RMSE (Mg ha^{-1})	0.97	0.98	1.61
Test R-squared	0.45	0.36	0.65

Figure 4. Scatter plot of the predicted and actual AGB (Mg ha^{-1}) values for: (**A**) spring, (**B**) fall, and (**C**) multi-temporal models. Fitted lines with 95% interval indicators are shown in blue lines.

In the context of AGB regression in tidal marshes, the RF algorithm provides valuable insights into the relative importance of various features contributing to the estimation of AGB. A key advantage of this ensemble learning method is its ability to rank features based on their contribution to the model's predictive performance, known as feature importance. Feature importance in RF can be assessed using metrics such as Gini impurity or Mean Decrease in Impurity (MDI), which quantify the extent to which a specific feature contributes to the overall reduction in prediction error across all trees in the model. This information enables researchers to identify the most influential variables driving AGB dynamics in tidal marshes, determining the key biophysical, climatic, and hydrological factors that govern these ecosystems. Figure 5 depicts the importance of different features in AGB regression from Sentinel-1, -2, and SRTM.

In the context of feature importance analysis, it is observed that among the various features examined, the SWIR 1 and SWIR 2 bands (specifically, bands B11 and B12) obtained from Sentinel-2 data exhibit the highest level of significance. The SWIR spectral bands are crucial for wetland biomass estimation due to their sensitivity to vegetation. Less susceptible to atmospheric interference, SWIR bands excel in differentiating biomass components and mitigating shadow effects. Previous studies consistently affirm the effectiveness of SWIR in enhancing accuracy, underscoring its pivotal role in remote sensing applications for wetland ecological monitoring [68]. Notably, within the Sentinel-2 bands, the Red Edge 1 and RGB bands also demonstrate notable importance. Interestingly, the NDSI surprisingly demonstrates outstanding performance among the spectral indices, whereas NDVI exhibits an average level of importance. Although originally named as snow index, NDSI outperforms NDVI due to its utilization of the SWIR band. Unlike NDVI, which

relies on NIR, NDSI's incorporation of SWIR enhances its capability to distinguish between features like wetlands and water inundated areas, resulting in superior performance in wetland environments. With regard to SAR features, the feature "Span" displays the highest capability in AGB regression. The importance of different features displays a correlation in diverse seasonal and multi-temporal models.
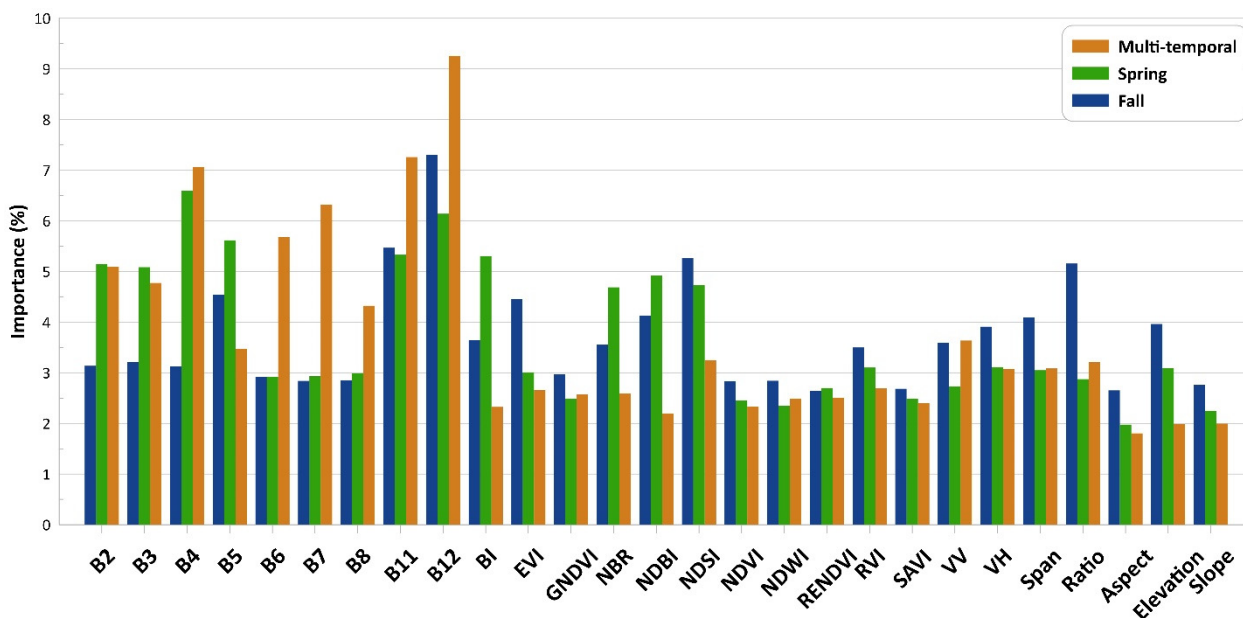

Figure 5. The importance of different features from the RF models.

3.2. Seasonal Models

In this study, AGB maps were produced on a large scale for spring and fall seasons, as the growing and sinking seasons. Figure 6 shows the results for the spring season. The spring period represents a vital stage in the vegetation growing season, as it corresponds to the onset of plant growth and development, driven by factors such as increasing temperatures, longer daylight hours, and nutrient availability. Coinciding with the peak of the spring river flood season, this period experiences elevated water levels, which can result in the widespread inundation of riparian and floodplain ecosystems. These flooding events contribute to the distribution of nutrients, sediment, and organic matter, thereby supporting the growth and proliferation of vegetation within these habitats. Consequently, AGB during the spring period is subjected to significant changes, as the interplay between hydrological dynamics and vegetation growth shapes the overall structure and composition of ecosystems. Monitoring and quantifying AGB during this critical phase is essential for understanding ecosystem dynamics, evaluating the impacts of environmental changes, and informing effective management and conservation strategies for these valuable natural resources.

In many ecosystems, August is considered the period of peak biomass, as it typically corresponds to the culmination of the growing season. AGB results for the fall season are illustrated in Figure 7. During this time, the vegetation already benefits from warmer temperatures, longer daylight hours, and nutrient availability throughout the growth period. As a result, plants reach their maximum biomass and structural complexity, providing essential habitat and resources for dependent species. Concurrently, August is often characterized by a period of low river discharge as the spring flood season has subsided and water levels have returned to normal or below-average levels. This reduction in river discharge can contribute to the stabilization of soil and sediment, promoting further vegetation growth and consolidation of the accumulated biomass. The combination of these factors results in the high AGB values observed during this time of the year. Gaining insight into and measuring biomass during the period of maximum vegetation growth in August is of utmost importance. This endeavor is critical in evaluating the well-being of

ecosystems, assessing the consequences of environmental fluctuations, and guiding the development of efficient strategies for ecosystem management and conservation. Accurate monitoring of AGB during this critical phase can also provide valuable insights into the carbon stock potential of these ecosystems, as well as their capacity to support biodiversity and contribute to overall ecosystem functioning.
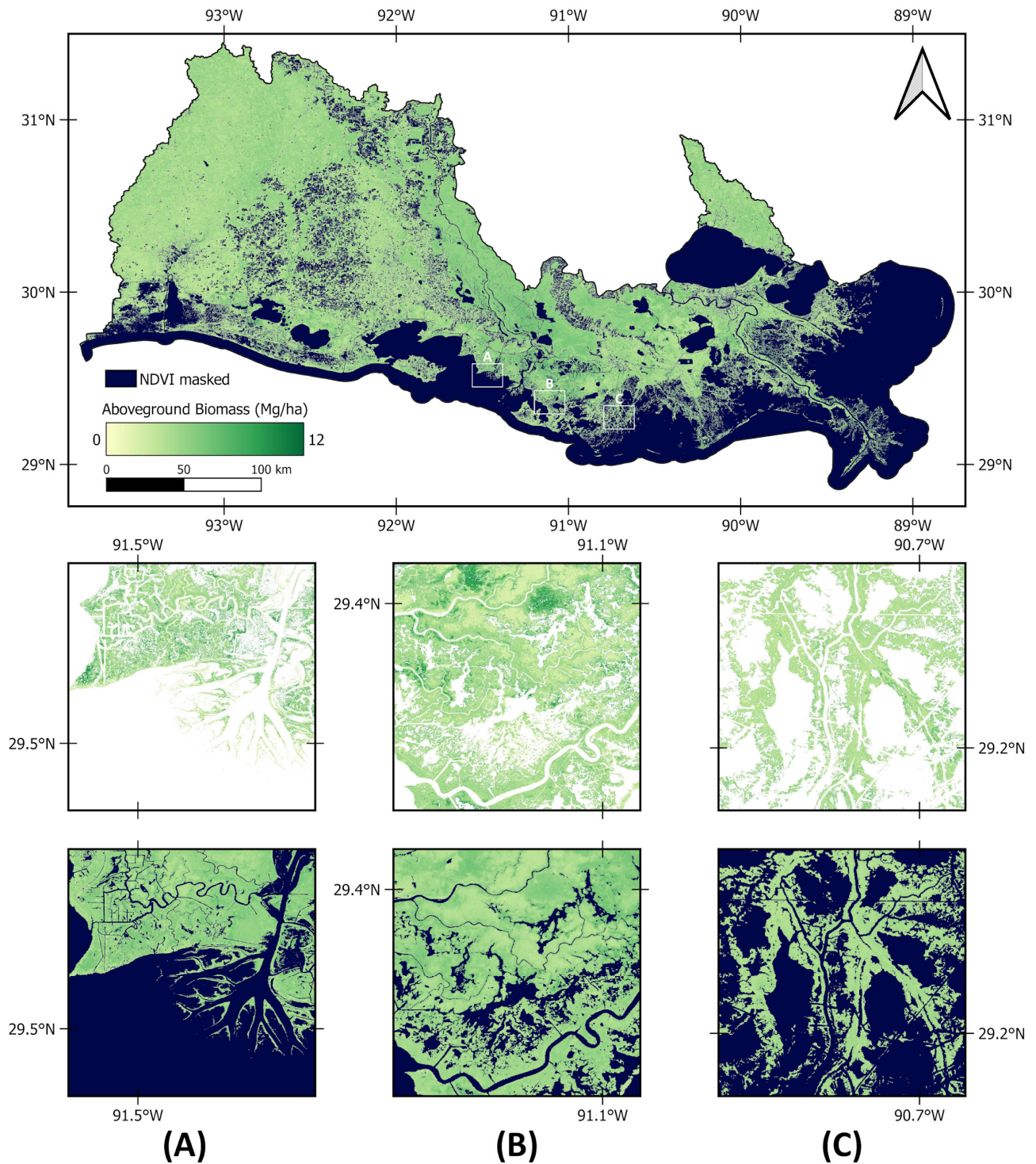

Figure 6. AGB map of the spring season (March and April 2021) and zoomed maps of (**A–C**) regions. The first row shows results from AVIRIS-NG (small-scale model), and the second row shows results from Sentinel-1 and -2 (large-scale model).
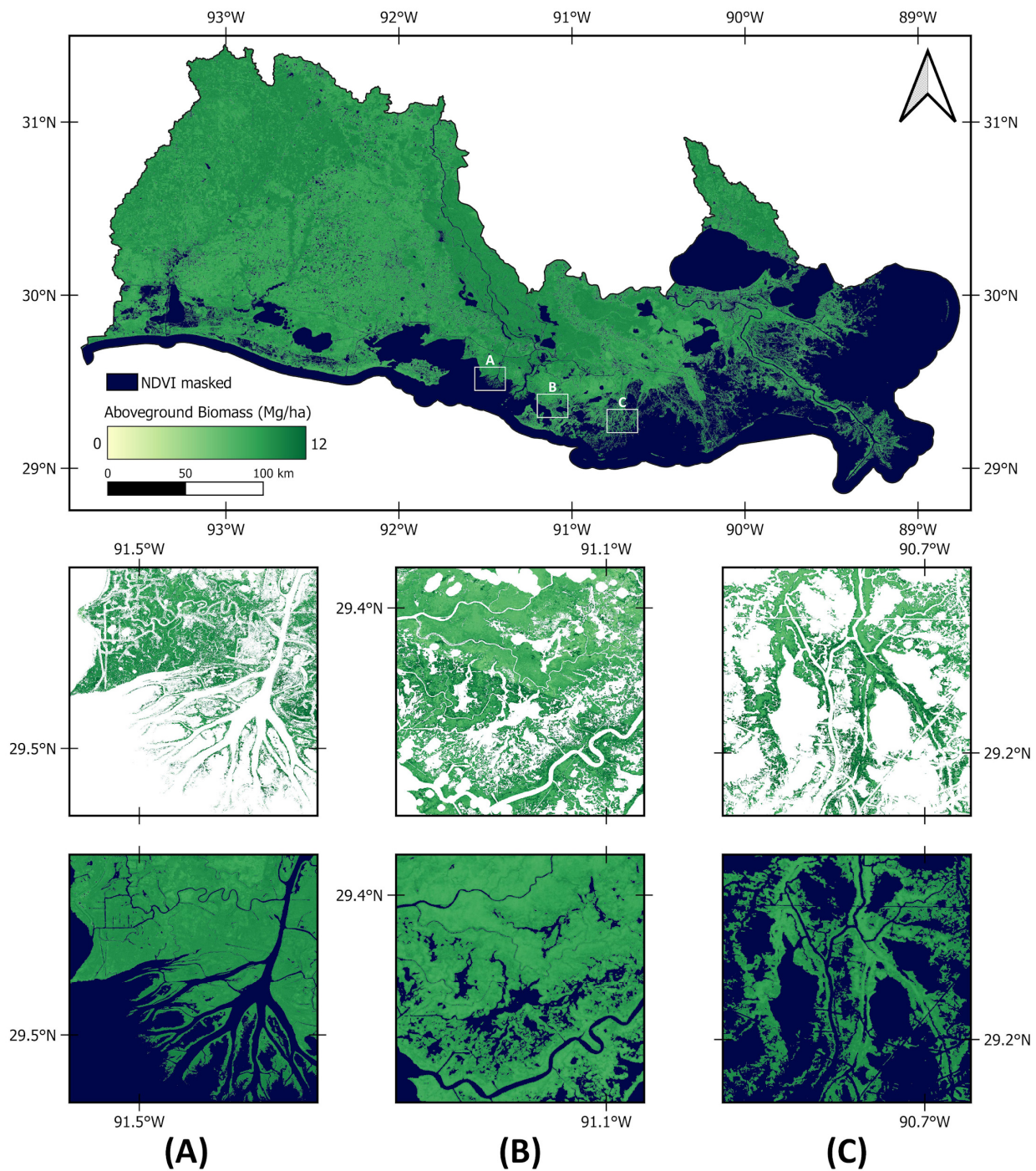
Figure 7. AGB map of the fall season (August 2021) and zoomed maps of (**A**–**C**) regions. The first row shows results from AVIRIS-NG (small-scale model), and the second row shows results from Sentinel-1 and -2 (large-scale model).

3.3. Multi-Temporal Model

The phenology of AGB in tidal wetlands plays a pivotal role in understanding the temporal dynamics of these ecosystems, as well as their capacity for carbon stock throughout the year. Tidal wetlands, encompassing marshes, mangroves, and seagrass meadows, are highly productive ecosystems that contribute significantly to global carbon storage. AGB phenology in these habitats is governed by complex interactions between hydrological, climatic, and biotic factors, which shape the growth, senescence, and decomposition of

plant biomass across different seasons. The monthly results of the AGB derived from multi-temporal model are shown in Figure 8.
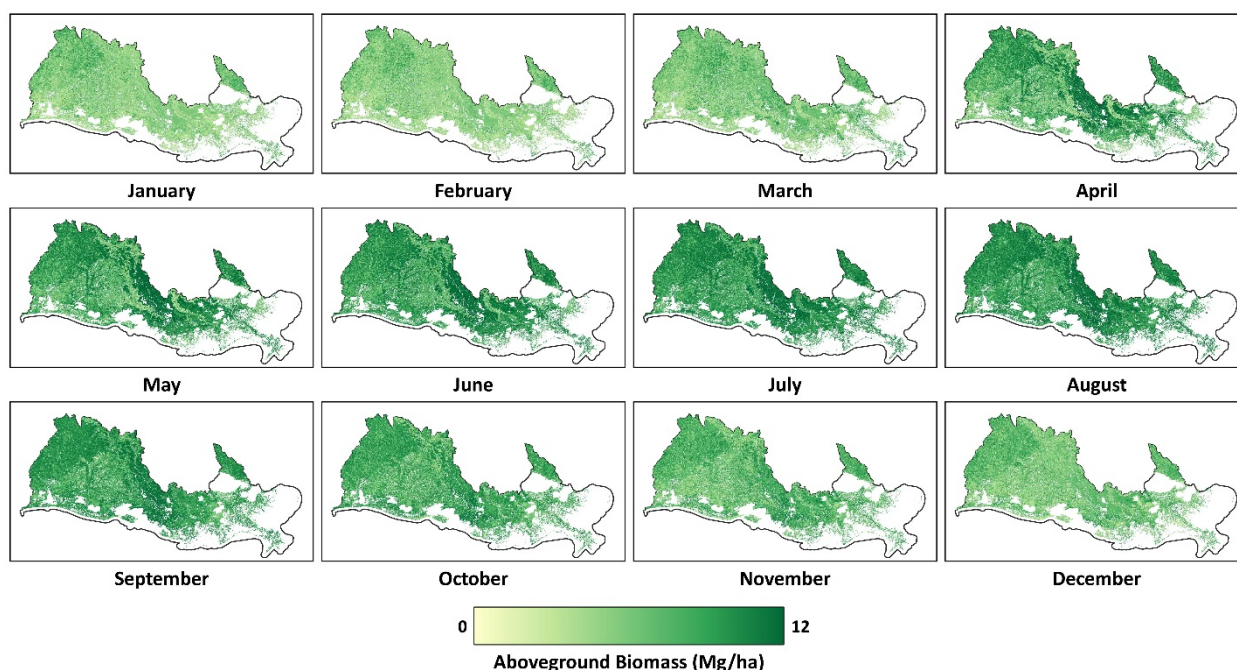

January   **February**   **March**   **April**

May   **June**   **July**   **August**

September   **October**   **November**   **December**

0 — 12
Aboveground Biomass (Mg/ha)

Figure 8. AGB monthly maps produced using the multi-temporal model.

Carbon stock in tidal wetlands relies heavily on the accumulation and preservation of organic matter, primarily derived from the AGB of vegetation. March marks the beginning of the growing season, as the low trend of AGB in January and February start the beginning of the uptrend. During the growing season, as plants photosynthesize and accumulate biomass, they assimilate atmospheric carbon dioxide, converting it into organic carbon. There is a sharp contrast between the AGB values in April and March, showing the growth of the AGB in summer. This trend continues until August, when the AGB map reaches the highest values and saturation. As plant material dies and decomposes, a portion of this carbon is incorporated into the soil, leading to long-term storage. The rate and magnitude of carbon stock in tidal wetlands can vary significantly throughout the year due to fluctuations in AGB phenology, reflecting changes in growth rates, plant productivity, and decomposition processes. Starting from September and after the peak biomass in the fall season, the down trend of AGB begins and continues into the winter. Furthermore, the produced monthly maps derived from the multi-temporal model in March and August confirm the previous results from the spring and fall seasons. This shows the consistency and novelty of the multi-temporal model, as the results have integrity with seasonal spring and fall models.

By closely examining the phenology of AGB in tidal wetlands and its association with carbon stock dynamics, researchers can gain valuable insights into the factors that influence the carbon storage capacity of these ecosystems. This understanding is crucial for informing management and conservation strategies aimed at preserving and enhancing the carbon stock potential of tidal wetlands, as well as their role in mitigating climate change and supporting biodiversity. Figure 9 presents an illustration of the mean AGB across various wetland classifications during each month, measured in megagrams per hectare (Mg ha^{-1}). Freshwater forested shrub wetlands exhibited the highest average AGB, and their values exhibited a significant increase during the growing season, peaking at maximum levels between May and August, followed by a gradual decline. The estimated biomass for freshwater forested shrub wetlands accounted for a substantial portion of this region, reaching a maximum of 1,092,480 megagrams. Notably, freshwater emergent wetlands

followed a similar temporal pattern to the forested shrub wetlands, with peak averages observed in June and a subsequent decrease beginning in August. Conversely, estuarine and marine wetlands demonstrated the lowest average biomass, exhibiting the most substantial fluctuations in AGB throughout the year. Furthermore, both freshwater forested shrub wetlands and estuarine and marine wetlands contributed a smaller proportion to the overall AGB, measuring 400,746 and 489,972 Mg, respectively.
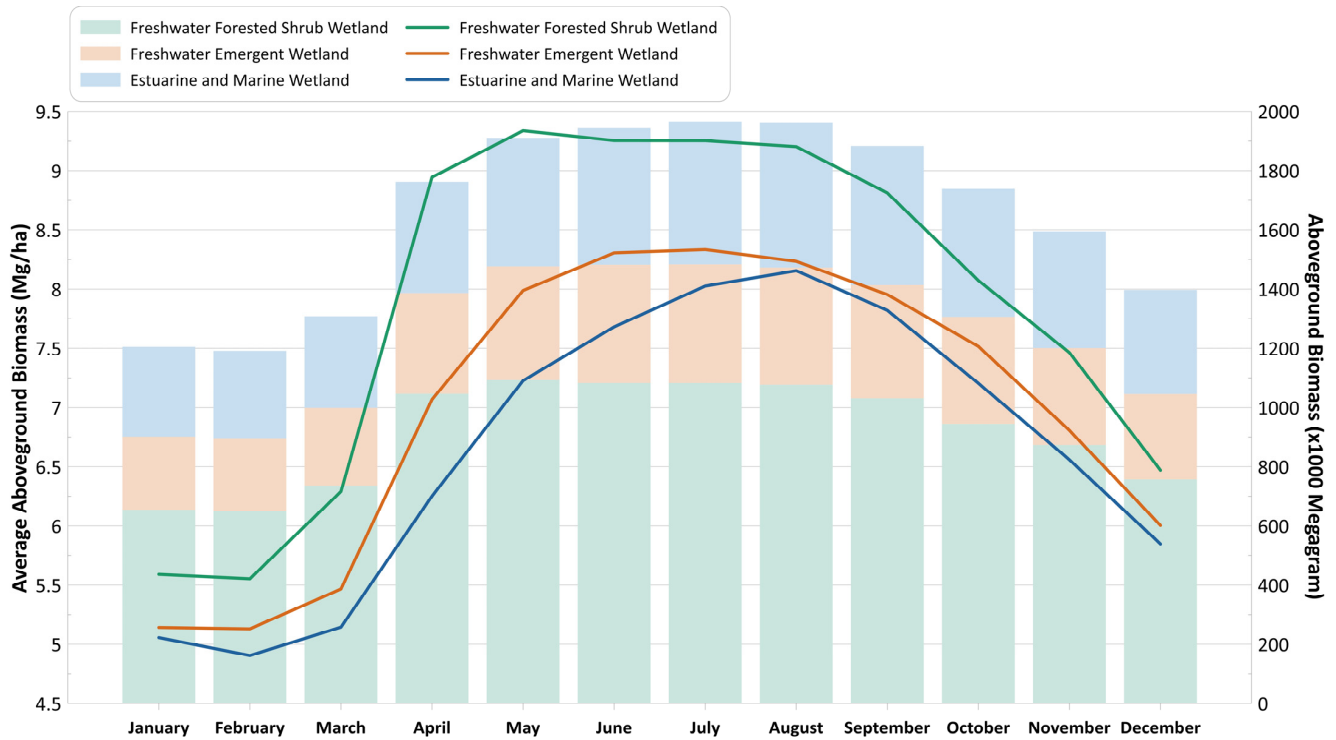

Figure 9. Average AGB (lines) and estimated total AGB (bars) for each wetland class in the region.

4. Discussion

A comprehensive multi-level remote sensing model of aboveground tidal marsh biomass was developed for the MRD region and southern Louisiana that can be applied to a variety of saline, brackish, and freshwater marshes, and wetlands. The researchers used the collected regional dataset of the AGB of tidal wetlands from the MRD to accomplish this goal. Our objective was to determine whether a repeatable remote sensing methodology could be used to estimate AGB in the tidal marsh that was consistent, transferable, free, or low-cost, and applicable to different estuarine conditions. To estimate the biomass of tidal marshes, researchers used multi-platform data to develop a robust and scalable remote sensing model.

AGB is a crucial metric in understanding the health and productivity of ecosystems, as it quantifies the living organic material found above the soil surface, primarily consisting of plant structures such as stems, leaves, and branches. The study's key findings lay in its innovative multi-scale approach, effectively translating field measurements to local and regional scales using both airborne and spaceborne platforms. Leveraging the advantageous attributes of spaceborne data, the study successfully bridged the gap between small-scale models derived from airborne data and large-scale estimations. Furthermore, the utilization of multi-temporal data proved instrumental in capturing the intra-annual variation of coastal wetland biomass, enabling the creation of monthly maps that provide a comprehensive depiction of the biomass dynamics over time. These key findings emphasize the feasibility of a multi-sourced, multi-scaled approach in achieving a holistic understanding of coastal wetland biomass and its temporal variations, addressing a crucial gap in the field.

The production of accurate and reliable AGB maps and analyses holds paramount importance for various aspects of ecosystem management, strategy planning, decision making, environmental conservation, and a range of potential applications. AGB maps provide crucial information about the spatial distribution and temporal dynamics of vegetation biomass, enabling informed decision-making processes related to land use, resource management, and conservation efforts. These maps serve as valuable tools for monitoring ecosystem health, assessing carbon stocks, evaluating the impacts of environmental changes, and predicting future vegetation growth patterns. Moreover, the availability of high-quality AGB data facilitates the development of effective management strategies for sustainable land use, biodiversity conservation, and climate change mitigation initiatives. Therefore, the generation and analysis of AGB maps play a pivotal role in advancing scientific understanding and promoting evidence-based management practices across various disciplines.

Compared to previous research conducted within this region, the findings of this study demonstrated marked advancements in resolution, coverage, and accuracy. In a comprehensive prior investigation spanning the United States, the examination involved the application of Sentinel-1 C-band SAR, Landsat, and the National Agriculture Imagery Program (NAIP) for wetland AGB estimation [69]. The study resulted in the production of an AGB map for the Mississippi Delta, exhibiting a spatial resolution of 30 m and an RMSE of 479 g/m^2. By integrating multi-source Sentinel-1 and Sentinel-2 data, this research heightened the resolution of the wetland AGB map to 10 m, enhancing the level of detail presented. The achieved RMSE values of 293.83 g/m^2 at a smaller scale and 160.97 g/m^2 in the larger scale model substantially bolstered the accuracy of the AGB maps, offering more dependable outcomes. Additionally, another study utilizing AVIRIS-NG and UAVSAR managed to produce AGB maps with an RMSE of 109.24 g/m^2, albeit for a restricted area (one of six field sites; [43]). Despite the relatively superior accuracy attained in this present study, limitations persist due to the absence of large-scale maps and the elevated costs associated with data acquisition, constraining the wider application of AGB maps.

Estimating AGB in tidal marshes presents unique challenges, primarily due to the dynamic nature of these ecosystems and the complex interactions among their biotic and abiotic components. Field data collection poses a significant challenge in accurately quantifying AGB, requiring repeated measurements to capture the temporal changes in AGB accurately. The availability of longitudinal data is crucial for a comprehensive understanding of AGB dynamics and for developing robust models that can account for the variability in biomass accumulation and decomposition processes over time. Additionally, the development of larger-scale AGB estimation models necessitate a greater volume of field data, encompassing diverse tidal marsh ecosystems, to enhance the model's reliability and generalizability. Therefore, a comprehensive and extensive collection of field data is essential for improving the accuracy and applicability of AGB estimation in tidal marshes. In addition to optical and SAR data, the utilization of other spatial data, such as biophysical parameters, can provide valuable insights into the complex relationships between AGB and environmental factors. Incorporating these additional data sources, including climate data, topographic variables, and soil properties, can enhance the accuracy and precision of AGB estimation models. Moreover, the emergence of deep learning techniques offers promising avenues for developing more sophisticated and comprehensive models for AGB estimation. Deep learning models have the capability to capture intricate patterns and relationships in large and complex datasets, enabling the integration of diverse data sources and the extraction of high-level features that may improve AGB estimation accuracy [70]. By harnessing the potential of these advanced techniques and incorporating additional spatial data, future research endeavors can advance our understanding of AGB dynamics in tidal marshes and contribute to more effective management and conservation strategies in these ecologically significant ecosystems.

5. Conclusions

In this study, a comprehensive and innovative multi-scale approach was introduced to combine field data with aerial and satellite imagery for the estimation of AGB in coastal wetlands. By leveraging the synergistic use of radar and optical data from Sentinel-1 and -2, AGB maps with a spatial resolution of 10 m were generated for the Louisiana coastal wetlands. The utilization of the multi-scale and multi-temporal approach and RF machine learning technique enabled the development of distinct models for the spring, fall, and multi-temporal, facilitating the precise measurement of the onset of the growing season and the peak biomass period. Additionally, the multi-temporal model allowed for continuous monitoring of the phenology of coastal wetlands throughout the year, elucidating the temporal patterns of AGB. Rigorous evaluation of each individual model using a holdout dataset, comprising 30% of the data untouched during training, yielded compelling results. Notably, the spring model achieved a RMSE of 0.97 Mg ha^{-1}, the fall model attained an RMSE of 0.98 Mg ha^{-1}, and the multi-temporal model yielded an RMSE of 1.61 Mg ha^{-1}. Investigating the outputs of the RF models revealed the significance of various features, including short-wave infrared bands, RGB bands, vegetation indices, and polarimetric features, in AGB estimation. The produced AGB maps hold immense value for decision-makers at various levels, ranging from local to federal governments, in their efforts to protect and restore coastal wetlands and mitigate potential damage. Furthermore, these maps serve as invaluable tools for environmental management and strategy planning. Future research can effectively address the constraint posed by the scarcity of ground reference data through the application of cutting-edge deep learning methodologies and innovative data expansion techniques.

References

1. Mcleod, E.; Chmura, G.L.; Bouillon, S.; Salm, R.; Björk, M.; Duarte, C.M.; Lovelock, C.E.; Schlesinger, W.H.; Silliman, B.R. A blueprint for blue carbon: Toward an improved understanding of the role of vegetated coastal habitats in sequestering CO_2. *Front. Ecol. Environ.* **2011**, *9*, 552–560. [CrossRef] [PubMed]
2. Pendleton, L.; Donato, D.C.; Murray, B.C.; Crooks, S.; Jenkins, W.A.; Sifleet, S.; Craft, C.; Fourqurean, J.W.; Kauffman, J.B.; Marbà, N.; et al. Estimating Global "Blue Carbon" Emissions from Conversion and Degradation of Vegetated Coastal Ecosystems. *PLoS ONE* **2012**, *7*, e43542. [CrossRef] [PubMed]
3. Intergovernmental Panel on Climate Change. *Climate Change 2014: Mitigation of Climate Change: Working Group III Contribution to the IPCC Fifth Assessment Report*, 1st ed.; Cambridge University Press: Cambridge, UK, 2015; ISBN 978-1-107-05821-7.
4. Bridgham, S.D.; Megonigal, J.P.; Keller, J.K.; Bliss, N.B.; Trettin, C. The carbon balance of North American wetlands. *Wetlands* **2006**, *26*, 889–916. [CrossRef]
5. Wylie, L.; Sutton-Grier, A.E.; Moore, A. Keys to successful blue carbon projects: Lessons learned from global case studies. *Mar. Policy* **2016**, *65*, 76–84. [CrossRef]

6. Howard, J.; Sutton-Grier, A.; Herr, D.; Kleypas, J.; Landis, E.; Mcleod, E.; Pidgeon, E.; Simpson, S. Clarifying the role of coastal and marine systems in climate mitigation. *Front. Ecol. Environ.* **2017**, *15*, 42–50. [CrossRef]

7. Duarte, C.M.; Losada, I.J.; Hendriks, I.E.; Mazarrasa, I.; Marbà, N. The role of coastal plant communities for climate change mitigation and adaptation. *Nat. Clim. Chang.* **2013**, *3*, 961–968. [CrossRef]

8. Kouhgardi, E.; Hemati, M.; Shakerdargah, E.; Shiri, H.; Mahdianpari, M. Monitoring Shoreline and Land Use/Land Cover Changes in Sandbanks Provincial Park Using Remote Sensing and Climate Data. *Water* **2022**, *14*, 3593. [CrossRef]

9. Kelleway, J.J.; Serrano, O.; Baldock, J.A.; Burgess, R.; Cannard, T.; Lavery, P.S.; Lovelock, C.E.; Macreadie, P.I.; Masqué, P.; Newnham, M.; et al. A national approach to greenhouse gas abatement through blue carbon management. *Glob. Environ. Chang.* **2020**, *63*, 102083. [CrossRef]

10. Needelman, B.A.; Emmer, I.M.; Emmett-Mattox, S.; Crooks, S.; Megonigal, J.P.; Myers, D.; Oreska, M.P.J.; McGlathery, K. The Science and Policy of the Verified Carbon Standard Methodology for Tidal Wetland and Seagrass Restoration. *Estuaries Coasts* **2018**, *41*, 2159–2171. [CrossRef]

11. Holmquist, J.R.; Windham-Myers, L.; Bliss, N.; Crooks, S.; Morris, J.T.; Megonigal, J.P.; Troxler, T.; Weller, D.; Callaway, J.; Drexler, J.; et al. Accuracy and Precision of Tidal Wetland Soil Carbon Mapping in the Conterminous United States. *Sci. Rep.* **2018**, *8*, 9478. [CrossRef] [PubMed]

12. Wilen, B.O.; Bates, M.K. The US Fish and Wildlife Service's National Wetlands Inventory Project. In *Classification and Inventory of the World's Wetlands*; Finlayson, C.M., van der Valk, A.G., Eds.; Springer: Dordrecht, The Netherlands, 1995; pp. 153–169. ISBN 978-94-010-4190-4.

13. IPCC. *Good Practice Guidance for Land Use, Land-Use Change and Forestry/The Intergovernmental Panel on Climate Change*; Penman, J., Ed.; IPCC: Hayama, Japan, 2003; ISBN 978-4-88788-003-0.

14. Gonzalez, P.; Asner, G.P.; Battles, J.J.; Lefsky, M.A.; Waring, K.M.; Palace, M. Forest carbon densities and uncertainties from Lidar, QuickBird, and field measurements in California. *Remote Sens. Environ.* **2010**, *114*, 1561–1575. [CrossRef]

15. Pettorelli, N.; Laurance, W.F.; O'Brien, T.G.; Wegmann, M.; Nagendra, H.; Turner, W. Satellite remote sensing for applied ecologists: Opportunities and challenges. *J. Appl. Ecol.* **2014**, *51*, 839–848. [CrossRef]

16. NOAA Office for Coastal Management. *NOAA Coastal Change Analysis Program (C-CAP) Regional Land Cover Database 2015*; NOAA Office for Coastal Management: Charleston, SC, USA, 2015.

17. Hemati, M.; Mahdianpari, M.; Shiri, H.; Mohammadimanesh, F. Comprehensive Landsat-Based Analysis of Long-Term Surface Water Dynamics over Wetlands and Waterbodies in North America. *Can. J. Remote Sens.* **2023**, *50*, 2293058. [CrossRef]

18. Hemati, M.; Hasanlou, M.; Mahdianpari, M.; Mohammadimanesh, F. A Systematic Review of Landsat Data for Change Detection Applications: 50 Years of Monitoring the Earth. *Remote Sens.* **2021**, *13*, 2869. [CrossRef]

19. Berger, M.; Moreno, J.; Johannessen, J.A.; Levelt, P.F.; Hanssen, R.F. ESA's sentinel missions in support of Earth system science. *Remote Sens. Environ.* **2012**, *120*, 84–90. [CrossRef]

20. Hemati, M.; Hasanlou, M.; Mahdianpari, M.; Mohammadimanesh, F. Iranian wetland inventory map at a spatial resolution of 10 m using Sentinel-1 and Sentinel-2 data on the Google Earth Engine cloud computing platform. *Environ. Monit. Assess.* **2023**, *195*, 558. [CrossRef]

21. Mahdianpari, M.; Brisco, B.; Granger, J.; Mohammadimanesh, F.; Salehi, B.; Homayouni, S.; Bourgeau-Chavez, L. The Third Generation of Pan-Canadian Wetland Map at 10 m Resolution Using Multisource Earth Observation Data on Cloud Computing Platform. *IEEE J. Sel. Top. Appl. Earth Obs. Remote Sens.* **2021**, *14*, 8789–8803. [CrossRef]

22. Gorelick, N.; Hancher, M.; Dixon, M.; Ilyushchenko, S.; Thau, D.; Moore, R. Google Earth Engine: Planetary-scale geospatial analysis for everyone. *Remote Sens. Environ.* **2017**, *202*, 18–27. [CrossRef]

23. Tamiminia, H.; Salehi, B.; Mahdianpari, M.; Quackenbush, L.; Adeli, S.; Brisco, B. Google Earth Engine for geo-big data applications: A meta-analysis and systematic review. *ISPRS J. Photogramm. Remote Sens.* **2020**, *164*, 152–170. [CrossRef]

24. Bai, T.; Wang, L.; Yin, D.; Sun, K.; Chen, Y.; Li, W.; Li, D. Deep learning for change detection in remote sensing: A review. *Geo-Spat. Inf. Sci.* **2023**, *26*, 262–288. [CrossRef]

25. Hemati, M.; Mahdianpari, M.; Hasanlou, M.; Mohammadimanesh, F. Iranian Wetland Hydroperiod Change Detection Using an Unsupervised Method on 20 Years of Landsat Data Within the Google Earth Engine. In Proceedings of the IGARSS 2022—2022 IEEE International Geoscience and Remote Sensing Symposium, Kuala Lumpur, Malaysia, 17–22 July 2022; pp. 6209–6212.

26. Pasquarella, V.J.; Arévalo, P.; Bratley, K.H.; Bullock, E.L.; Gorelick, N.; Yang, Z.; Kennedy, R.E. Demystifying LandTrendr and CCDC temporal segmentation. *Int. J. Appl. Earth Obs. Geoinf.* **2022**, *110*, 102806. [CrossRef]

27. Mutanga, O.; Adam, E.; Cho, M.A. High density biomass estimation for wetland vegetation using WorldView-2 imagery and random forest regression algorithm. *Int. J. Appl. Earth Obs. Geoinf.* **2012**, *18*, 399–406. [CrossRef]

28. González Trilla, G.; Pratolongo, P.; Beget, M.E.; Kandus, P.; Marcovecchio, J.; Di Bella, C. Relating Biophysical Parameters of Coastal Marshes to Hyperspectral Reflectance Data in the Bahia Blanca Estuary, Argentina. *J. Coast. Res.* **2013**, *286*, 231–238. [CrossRef]

29. Byrd, K.B.; Windham-Myers, L.; Leeuw, T.; Downing, B.; Morris, J.T.; Ferner, M.C. Forecasting Tidal Marsh Elevation and Habitat Change through Fusion of Earth Observations and a Process Model. *Ecosphere* **2016**, *7*, e01582. [CrossRef]

30. Ghosh, S.; Mishra, D.R.; Gitelson, A.A. Long-Term Monitoring of Biophysical Characteristics of Tidal Wetlands in the Northern Gulf of Mexico—A Methodological Approach Using MODIS. *Remote Sens. Environ.* **2016**, *173*, 39–58. [CrossRef]

31. Schalles, J.; Hladik, C.; Lynes, A.; Pennings, S. Landscape Estimates of Habitat Types, Plant Biomass, and Invertebrate Densities in a Georgia Salt Marsh. *Oceanog* **2013**, *26*, 88–97. [CrossRef]

32. Lobell, D.B.; Thau, D.; Seifert, C.; Engle, E.; Little, B. A scalable satellite-based crop yield mapper. *Remote Sens. Environ.* **2015**, *164*, 324–333. [CrossRef]

33. Glenn, E.; Huete, A.; Nagler, P.; Nelson, S. Relationship Between Remotely-sensed Vegetation Indices, Canopy Attributes and Plant Physiological Processes: What Vegetation Indices Can and Cannot Tell Us About the Landscape. *Sensors* **2008**, *8*, 2136–2160. [CrossRef]

34. Liu, C.; Tao, R.; Li, W.; Zhang, M.; Sun, W.; Du, Q. Joint Classification of Hyperspectral and Multispectral Images for Mapping Coastal Wetlands. *IEEE J. Sel. Top. Appl. Earth Obs. Remote Sens.* **2021**, *14*, 982–996. [CrossRef]

35. Nagler, P. Leaf area index and normalized difference vegetation index as predictors of canopy characteristics and light interception by riparian species on the Lower Colorado River. *Agric. For. Meteorol.* **2004**, *125*, 1–17. [CrossRef]

36. Mutanga, O.; Skidmore, A.K. Narrow band vegetation indices overcome the saturation problem in biomass estimation. *Int. J. Remote Sens.* **2004**, *25*, 3999–4014. [CrossRef]

37. Ollinger, S.V. Sources of variability in canopy reflectance and the convergent properties of plants. *New Phytol.* **2011**, *189*, 375–394. [CrossRef]

38. Langley, J.A.; Megonigal, J.P. Field-Based Radiometry to Estimate Tidal Marsh Plant Growth in Response to Elevated CO_2 and Nitrogen Addition. *Wetlands* **2012**, *32*, 571–578. [CrossRef]

39. Wang, Y.; Shen, X.; Tong, S.; Zhang, M.; Jiang, M.; Lu, X. Aboveground Biomass of Wetland Vegetation Under Climate Change in the Western Songnen Plain. *Front. Plant Sci.* **2022**, *13*, 941689. [CrossRef]

40. Woltz, V.L.; Stagg, C.L.; Byrd, K.B.; Windham-Myers, L.; Rovai, A.S.; Zhu, Z. Above- and Belowground Biomass Carbon Stock and Net Primary Productivity Maps for Tidal Herbaceous Marshes of the United States. *Remote Sens.* **2023**, *15*, 1697. [CrossRef]

41. Hemati, M.; Hasanlou, M.; Mahdianpari, M.; Mohammadimanesh, F. Wetland Mapping of Northern Provinces of Iran Using Sentinel-1 and Sentinel-2 in Google Earth Engine. In Proceedings of the 2021 IEEE International Geoscience and Remote Sensing Symposium IGARSS, Brussels, Belgium, 11–16 July 2021; pp. 96–99.

42. Aslan, A.; Rahman, A.F.; Warren, M.W.; Robeson, S.M. Mapping spatial distribution and biomass of coastal wetland vegetation in Indonesian Papua by combining active and passive remotely sensed data. *Remote Sens. Environ.* **2016**, *183*, 65–81. [CrossRef]

43. Jensen, D.; Cavanaugh, K.C.; Simard, M.; Okin, G.S.; Castañeda-Moya, E.; McCall, A.; Twilley, R.R. Integrating imaging spectrometer and synthetic aperture radar data for estimating wetland vegetation aboveground biomass in coastal Louisiana. *Remote Sens.* **2019**, *11*, 2533. [CrossRef]

44. Du, Y.; Wang, J.; Liu, Z.; Yu, H.; Li, Z.; Cheng, H. Evaluation on Spaceborne Multispectral Images, Airborne Hyperspectral, and LiDAR Data for Extracting Spatial Distribution and Estimating Aboveground Biomass of Wetland Vegetation Suaeda Salsa. *IEEE J. Sel. Top. Appl. Earth Obs. Remote Sens.* **2019**, *12*, 200–209. [CrossRef]

45. Sun, S.; Wang, Y.; Song, Z.; Chen, C.; Zhang, Y.; Chen, X.; Chen, W.; Yuan, W.; Wu, X.; Ran, X.; et al. Modelling aboveground biomass carbon stock of the bohai rim coastal wetlands by integrating remote sensing, terrain, and climate data. *Remote Sens.* **2021**, *13*, 4321. [CrossRef]

46. Wang, Z.H.; Dai, H.Y.; Liu, J.B.; Ren, J.T. Aboveground biomass estimation of caohai wetland vegetation based on optical and radar remote sensing. *UPB Sci. Bull. Ser. C Electr. Eng. Comput. Sci.* **2023**, *85*, 339–350.

47. Chen, C.; Ma, Y.; Ren, G.; Wang, J. Aboveground Biomass of Salt-Marsh Vegetation in Coastal Wetlands: Sample Expansion of in Situ Hyperspectral and Sentinel-2 Data Using a Generative Adversarial Network. *Remote Sens. Environ.* **2022**, *270*, 112885. [CrossRef]

48. Blount, T.; Silvestri, S.; Marani, M.; D'Alpaos, A. Lidar Derived Salt Marsh Topography and Biomass: Defining Accuracy and Spatial Patterns of Uncertainty. *Int. Arch. Photogramm. Remote Sens. Spatial Inf. Sci.* **2023**, 57–62. [CrossRef]

49. Eon, R.S.; Goldsmith, S.; Bachmann, C.M.; Tyler, A.C.; Lapszynski, C.S.; Badura, G.P.; Osgood, D.T.; Brett, R. Retrieval of salt marsh above-ground biomass from high-spatial resolution hyperspectral imagery using PROSAIL. *Remote Sens.* **2019**, *11*, 1385. [CrossRef]

50. Navarro, A.; Young, M.; Allan, B.; Carnell, P.; Macreadie, P.; Ierodiaconou, D. The Application of Unmanned Aerial Vehicles (UAVs) to Estimate above-Ground Biomass of Mangrove Ecosystems. *Remote Sens. Environ.* **2020**, *242*, 111747. [CrossRef]

51. Morgan, G.R.; Wang, C.; Morris, J.T. Rgb indices and canopy height modelling for mapping tidal marsh biomass from a small unmanned aerial system. *Remote Sens.* **2021**, *13*, 3406. [CrossRef]

52. Shlemon, R.J. *Subaqueous Delta Formation—Atchafalaya Bay, Louisiana*; Broussand, M.L., Ed.; Deltas-models for exploration, Houston Geological Society; Houston Geological Society: Houston, TX, USA, 1975; pp. 209–221.

53. Louis, J.; Debaecker, V.; Pflug, B.; Main-Knorn, M.; Bieniarz, J.; Mueller-Wilm, U.; Cadau, E.; Gascon, F. SENTINEL-2 SEN2COR: L2A Processor for Users. In Proceedings of the Living Planet Symposium 2016, Prague, Czech Republic, 9–13 May 2016; Ouwehand, L., Ed.; pp. 1–8.

54. Torres, R.; Snoeij, P.; Geudtner, D.; Bibby, D.; Davidson, M.; Attema, E.; Potin, P.; Rommen, B.; Floury, N.; Brown, M.; et al. GMES Sentinel-1 mission. *Remote Sens. Environ.* **2012**, *120*, 9–24. [CrossRef]

55. Jensen, D.; Cavanaugh, K.C.; Simard, M.; Christensen, A.; Rovai, A.; Twilley, R. Aboveground biomass distributions and vegetation composition changes in Louisiana's Wax Lake Delta. *Estuar. Coast. Shelf Sci.* **2021**, *250*, 107139. [CrossRef]

56. Castañeda-Moya, E.; Solohin, E. *Delta-X: Aboveground Biomass and Necromass across Wetlands, MRD, Louisiana, 2021*; ORNL DAAC: Oak Ridge, TN, USA, 2022. [CrossRef]

57. Green, R.O.; Eastwood, M.L.; Sarture, C.M.; Chrien, T.G.; Aronsson, M.; Chippendale, B.J.; Faust, J.A.; Pavri, B.E.; Chovit, C.J.; Solis, M.; et al. Imaging Spectroscopy and the Airborne Visible/Infrared Imaging Spectrometer (AVIRIS). *Remote Sens. Environ.* **1998**, *65*, 227–248. [CrossRef]

58. Thompson, D.R.; Cawse-Nicholson, K.; Erickson, Z.; Fichot, C.G.; Frankenberg, C.; Gao, B.-C.; Gierach, M.M.; Green, R.O.; Jensen, D.; Natraj, V.; et al. A unified approach to estimate land and water reflectances with uncertainties for coastal imaging spectroscopy. *Remote Sens. Environ.* **2019**, *231*, 111198. [CrossRef]

59. Greenberg, E.; Thompson, D.R.; Jensen, D.; Townsend, P.A.; Queally, N.; Chlus, A.; Fichot, C.G.; Harringmeyer, J.P.; Simard, M. An Improved Scheme for Correcting Remote Spectral Surface Reflectance Simultaneously for Terrestrial BRDF and Water-Surface Sunglint in Coastal Environments. *JGR Biogeosci.* **2022**, *127*, e2021JG006712. [CrossRef]

60. Queally, N.; Ye, Z.; Zheng, T.; Chlus, A.; Schneider, F.; Pavlick, R.; Townsend, P.A. FlexBRDF: A Flexible BRDF Correction for Grouped Processing of Airborne Imaging Spectroscopy Flightlines. *J. Geophys. Res. Biogeosci.* **2021**, *127*, e2021JG006622. [CrossRef]

61. Arasumani, M.; Singh, A.; Bunyan, M.; Robin, V.V. Testing the efficacy of hyperspectral (AVIRIS-NG), multispectral (Sentinel-2) and radar (Sentinel-1) remote sensing images to detect native and invasive non-native trees. *Biol. Invasions* **2021**, *23*, 2863–2879. [CrossRef]

62. Badola, A.; Panda, S.K.; Roberts, D.A.; Waigl, C.F.; Jandt, R.R.; Bhatt, U.S. A novel method to simulate AVIRIS-NG hyperspectral image from Sentinel-2 image for improved vegetation/wildfire fuel mapping, boreal Alaska. *Int. J. Appl. Earth Obs. Geoinf.* **2022**, *112*, 102891. [CrossRef]

63. Behera, M.D.; Barnwal, S.; Paramanik, S.; Das, P.; Bhattyacharya, B.K.; Jagadish, B.; Roy, P.S.; Ghosh, S.M.; Behera, S.K. Species-Level Classification and Mapping of a Mangrove Forest Using Random Forest—Utilisation of AVIRIS-NG and Sentinel Data. *Remote Sens.* **2021**, *13*, 2027. [CrossRef]

64. Mahdianpari, M.; Salehi, B.; Mohammadimanesh, F.; Motagh, M. Random forest wetland classification using ALOS-2 L-band, RADARSAT-2 C-band, and TerraSAR-X imagery. *ISPRS J. Photogramm. Remote Sens.* **2017**, *130*, 13–31. [CrossRef]

65. Breiman, L. Random forests. *Mach. Learn.* **2001**, *45*, 5–32. [CrossRef]

66. Jensen, D.J.; Castañeda-Moya, E.; Solohin, E.; Rovai, A.; Thompson, D.R.; Simard, M. *Delta-X: AVIRIS-NG L3 Derived Aboveground Biomass, MRD, Louisiana, USA, 2021, V2*; ORNL DAAC: Oak Ridge, TN, USA, 2023. [CrossRef]

67. Jensen, D.; Simard, M.; Thompson, D.R.; Solohin, E.; Castañeda-Moya, E. Towards consistent imaging spectroscopy-based global aboveground biomass retrievals in coastal wetlands across atmospheric states. In *AGU Fall Meeting Abstracts*; 2022; Volume 2022, Available online: https://ui.adsabs.harvard.edu/abs/2022AGUFMGC42D0745J/abstract (accessed on 1 December 2023).

68. Wan, R.; Wang, P.; Wang, X.; Yao, X.; Dai, X. Mapping Aboveground Biomass of Four Typical Vegetation Types in the Poyang Lake Wetlands Based on Random Forest Modelling and Landsat Images. *Front. Plant Sci.* **2019**, *10*, 1281. [CrossRef] [PubMed]

69. Byrd, K.B.; Ballanti, L.; Thomas, N.; Nguyen, D.; Holmquist, J.R.; Simard, M.; Windham-Myers, L. A remote sensing-based model of tidal marsh aboveground carbon stocks for the conterminous United States. *ISPRS J. Photogramm. Remote Sens.* **2018**, *139*, 255–271. [CrossRef]

70. Hosseiny, B.; Mahdianpari, M.; Hemati, M.; Radman, A.; Mohammadimanesh, F.; Chanussot, J. Beyond supervised learning in remote sensing: A systematic review of deep learning approaches. *IEEE J. Sel. Top. Appl. Earth Obs. Remote Sens.* **2023**, *17*, 1035–1052. [CrossRef]